

Fingerprinting the recovery of Antarctic ozone

<https://doi.org/10.1038/s41586-025-08640-9>

Received: 7 August 2024

Accepted: 13 January 2025

Published online: 5 March 2025

 Check for updates

Peidong Wang¹✉, Susan Solomon¹✉, Benjamin D. Santer^{2,3}, Douglas E. Kinnison⁴, Qiang Fu⁵, Kane A. Stone¹, Jun Zhang⁴, Gloria L. Manney^{6,7} & Luis F. Millán⁸

The Antarctic ozone ‘hole’ was discovered in 1985 (ref. 1) and man-made ozone-depleting substances (ODSs) are its primary cause². Following reductions of ODSs under the Montreal Protocol³, signs of ozone recovery have been reported, based largely on observations and broad yet compelling model–data comparisons⁴. Although such approaches are highly valuable, they do not provide rigorous statistical detection of the temporal and spatial structure of Antarctic ozone recovery in the presence of internal climate variability. Here we apply pattern-based detection and attribution methods as used in climate-change studies^{5–11} to separate anthropogenically forced ozone responses from internal variability, relying on trend pattern information as a function of month and height. The analysis uses satellite observations together with single-model and multi-model ensemble simulations to identify and quantify the month–height Antarctic ozone recovery ‘fingerprint’¹². We demonstrate that the data and simulations show compelling agreement in the fingerprint pattern of the ozone response to decreasing ODSs since 2005. We also show that ODS forcing has enhanced ozone internal variability during the austral spring, influencing detection of forced responses and their time of emergence. Our results provide robust statistical and physical evidence that actions taken under the Montreal Protocol to reduce ODSs are indeed resulting in the beginning of Antarctic ozone recovery, defined as increases in ozone consistent with expected month–height patterns.

Despite the decline in ODSs³, the continuing occurrence of large Antarctic ozone ‘holes’ in recent years—partly because of the 2020 Australian wildfire^{13–15} and 2022 Hunga volcanic eruption^{16–19}—along with concerns about a substantial decrease in October mid-stratospheric ozone²⁰, have stimulated discussion about the detectability of a robust signal in Antarctic ozone recovery. Formal detection and attribution (D&A) methods are needed to assess the effectiveness of the Montreal Protocol.

Initial-condition large ensembles (LEs) generated with fully coupled global climate models offer a unique opportunity to ‘fingerprint’ the anthropogenic influence. They provide valuable information on both natural internal variability and the characteristic space and time signatures of the climate responses to different external forcings^{5–12}. Such ensembles are rarely used in ozone studies, which generally apply multiple linear regression to isolate underlying forced trends by fitting ozone time series to known sources of variability (such as the solar cycle, El Niño–Southern Oscillation, quasi-biennial oscillation, volcanic activities etc.)²¹. By contrast, LEs do not require the assumption that the response is a linear combination of independent predictor variables²². Although some D&A methods have been applied to global ozone depletion and the time of emergence of total column recovery using multi-model ensembles^{23–25}, previous studies have not fully used the pattern-based D&A techniques. Furthermore, several members from

a single model that is well evaluated and realistic can reliably quantify modelled forced signals and intrinsic variability, whereas one run from each of a multi-model ensemble samples larger cross-model differences in forcing, response and variability²⁶, thus hampering the identification of the beginning of ozone recovery^{23,24}.

Observed and model-simulated ozone trends

We compare observed and simulated month–height trend patterns over 2005 to 2018 for Antarctic ozone, spatially averaged over 66° S–82° S (Fig. 1). Observations are from the Microwave Limb Sounder (MLS)²⁷. Model results are from two different sources: (1) the multi-model ensemble mean computed using one run of each of the 19 models that participated in phase 1 of the Chemistry–Climate Model Initiative (CCMI-1)²⁸; and (2) the single-model ensemble of ten different realizations of the Community Earth System Model–Whole Atmosphere Community Climate Model (CESM-WACCM; referred to as WACCM for short)^{29,30}. The WACCM (and some models in the CCMI) ensemble comprises free-running coupled ocean–atmosphere simulations forced by time-evolving changes in greenhouse gases (GHGs) and ODSs, referred to as the ‘refC2’ scenario (described in detail in Methods). We mainly focus on ozone trends from 2005 to 2018 (results covering

¹Department of Earth, Atmospheric, and Planetary Sciences, Massachusetts Institute of Technology, Cambridge, MA, USA. ²Physical Oceanography Department, Woods Hole Oceanographic Institution, Woods Hole, MA, USA. ³Joint Institute for Regional Earth System Science and Engineering, University of California, Los Angeles, Los Angeles, CA, USA. ⁴Atmospheric Chemistry Observations and Modeling, National Science Foundation National Center for Atmospheric Research, Boulder, CO, USA. ⁵Department of Atmospheric Sciences, University of Washington, Seattle, WA, USA. ⁶NorthWest Research Associates, Socorro, NM, USA. ⁷New Mexico Institute of Mining and Technology, Socorro, NM, USA. ⁸Jet Propulsion Laboratory, California Institute of Technology, Pasadena, CA, USA. [✉]e-mail: pdwang@mit.edu; solos@mit.edu

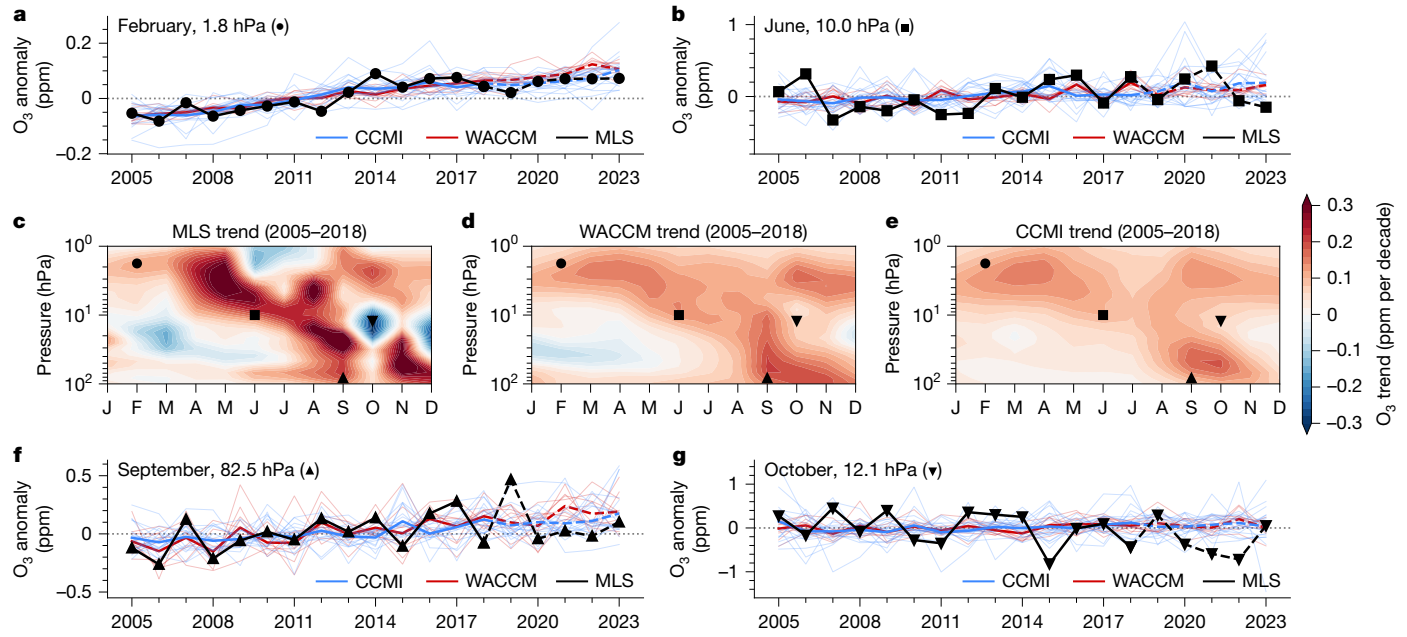


Fig. 1 | Month–height patterns of ozone trends in observations and simulations. The middle row shows the least-squares linear trends in ozone over 2005–2018 as a function of month and pressure in the MLS observations (c), the WACCM ten-member ensemble mean (d) and the CCMI 19-model ensemble mean (e). Results are for spatial averages over 66° S–82° S. We also show the time series of ozone anomalies (relative to the 2005–2018 mean) at four illustrative locations (indicated by different markers on the contour

figures) in February at 1.8 hPa (a), June at 10 hPa (b), September at 82.5 hPa (f) and October at 12.1 hPa (g). Thick blue and red lines are the model ensemble means and the thin lines are the ozone time series in individual model realizations. The black solid line is from the MLS. Time series after 2018 are shown as dashed lines because of probable impacts of exceptional perturbations from the 2019 sudden stratospheric warming, 2020 Australian wildfire and 2022 Hunga volcanic eruption.

longer periods are also considered below) to avoid recent exceptional events that are not represented in these models, including the 2019 sudden stratospheric warming³¹ and post-2020 wildfire and volcanic eruption mentioned earlier (note that the 2015 Calbuco eruption³² is also not generally simulated in these models but is included in our trend analysis). Time series used for calculating trends are presented for illustration for four selected months and heights in Fig. 1a,b,f,g; the expected post-2018 differences between observations and simulations are marked with dashed lines (in later figures as well).

Compared with the single real-world realization provided by the MLS, the modelled mean trends in the WACCM and CCMI have smaller amplitudes (Fig. 1c,d,e). This is partly because of the fact that the model ensemble means are averages over many different realizations with varying phasing of internal variability (which is uncorrelated, except by chance) superimposed on the forced response. For comparison, Extended Data Fig. 1 shows the ozone trends in 2005–2018 from individual WACCM realizations and CCMI model runs. Some individual members show month–height trend patterns that are more similar to the MLS, whereas others are less similar, reflecting differences in the phasing of internal variability. Nonetheless, nearly all realizations preserve some common features, reflecting the ‘fingerprint’ of GHG and ODS forcings on ozone trends.

Increases in lower-stratospheric ozone (at altitudes below the pressure level of approximately 30 hPa) during the austral spring are mainly because of the reduction in ODS concentrations³, leading to less heterogeneous ozone loss². The seasonal signature of the ozone hole in August–December is apparent in this region. Increases in upper-stratospheric ozone (above about 10 hPa) are partly the result of cooling caused by increasing GHGs (mainly CO₂)³³ and its effect on temperature-dependent ozone photochemistry³⁴. They are also partly the result of less reactive chlorine, through its effect on the ClO + O reaction that peaks near 40 km (ref. 35) (see Extended Data Fig. 2). In the descending circulation of the polar winter, the increased ozone in the upper stratosphere propagates down to the mid-stratosphere. This combined

month-resolved and height-resolved pattern characterizes the ‘fingerprint’ of GHG and ODS forcings on Antarctic ozone changes. In this study, we define ozone recovery as statistically significant increases in ozone that show these characteristic time–space fingerprints.

Noise of ozone variability and ODS forcing

Signal-to-noise (S/N) analyses in D&A climate studies typically use natural internal variability (‘noise’) estimated from long pre-industrial control runs^{5–11}. We rely on several noise estimates here from different WACCM scenarios (described in detail in Methods). Figure 2a,b shows the month–height patterns of noise, defined as the standard deviations of ozone trends in the two separate ten-member WACCM historical and refC2 ensembles (after first removing the mean forced response). Although generated with the same physical climate model, the magnitude of noise trends in the historical and refC2 simulations exhibits notable differences. This is especially important in the austral spring in the lower stratosphere, in which the ozone ‘hole’ typically occurs. The historical scenario has low GHGs and low ODSs, representing atmospheric conditions before the onset of large ozone losses in the 1980s. The refC2 scenario has high GHGs and high ODSs, comparable with present-day conditions. This indicates that the forcing differences in the two scenarios directly affect internal noise. It is important to account for forced changes in variability when examining ozone recovery—the estimated statistical significance of the observed trends can be affected by changes in noise amplitude.

There is a notable enhancement in ozone variability under the present-day high ODS conditions in austral spring in the lower stratosphere (marked with the white dashed boxes in Fig. 2a,b); the standard deviations in the refC2 and fGHG scenarios (low GHGs but high ODSs) are both increased by about 130% compared with the historical scenario. GHG forcing alone (the fODS scenario, with low ODSs but high GHGs) yields a narrow spread in ozone variability similar to the historical case, confirming that the variability enhancement is primarily driven by ODS

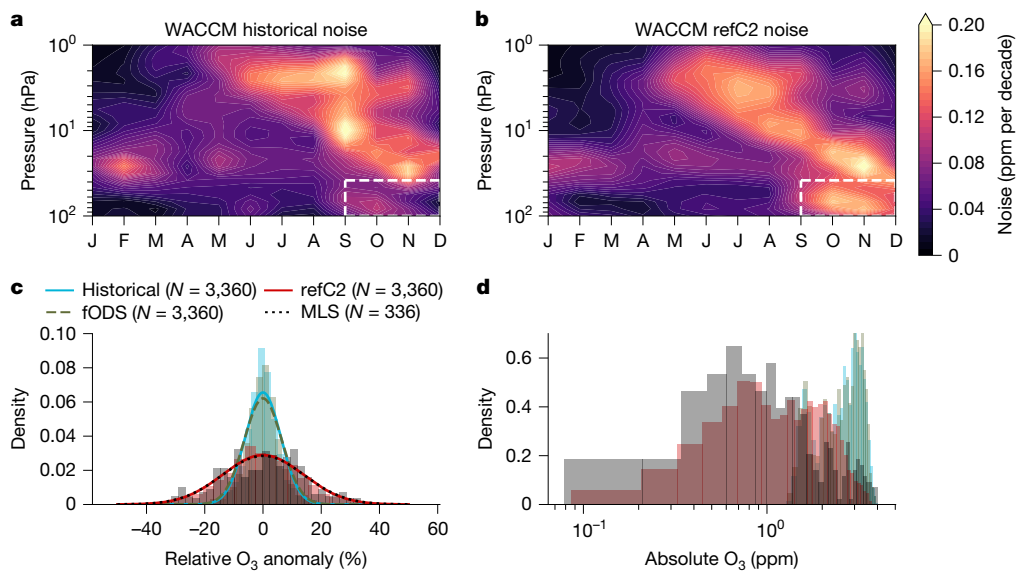


Fig. 2 | Ozone variability modulated by external forcing. Panels **a** and **b** show the month-height patterns of the standard deviation of ozone trends (averaged over 66° S–82° S) in the WACCM historical and refC2 scenarios, after first removing the ensemble mean. The standard deviation is a measure of the trend uncertainty arising from internal variability among the ten WACCM ensemble members. Both scenarios have the same trend length of 14 years: the historical scenario analysis period is from 1955 to 1968 and the refC2 analysis period is from 2005 to 2018. Panel **c** shows (for the white dashed boxes in the top panels) the residual internal variability in the WACCM and MLS ozone after

first removing the mean forced response of monthly mean ozone. Results are expressed as percent changes relative to the MLS annual mean climatology. The thick lines are the Gaussian fits to the distributions. Panel **d** shows the same data as in panel **c** but in terms of the absolute monthly ozone mixing ratios. The number of data points in each distribution is indicated in the legend. A similar figure for CCMI models is shown in Extended Data Fig. 3; although the noise pattern is qualitatively similar to that of the WACCM, the CCMI multi-model ensemble also reflects different model responses to forcing that can inflate noise compared with a single-model ensemble.

forcing. Such enhancement occurs because chemical ozone loss owing to ODSs acts in the same direction as the natural variations in ozone arising from Brewer–Dobson circulation variability. For example, a weak Brewer–Dobson circulation associated with negative ozone and negative temperature anomalies favours more heterogeneous ozone loss in the presence of high ODSs, extending the lower tail of the distribution of absolute ozone concentration³⁶ (Fig. 2d) and broadening ozone variability.

For accurate analysis of the statistical significance of ozone changes, it is critical that the model-based noise is realistic. Figure 2c shows the distributions of monthly mean ozone anomalies from the MLS and WACCM (after first removing the mean forced response) relative to the present-day MLS climatology, in the region highlighted by the white dashed boxes in Fig. 2a,b. The same data are shown in Fig. 2d in terms of absolute ozone mixing ratios. The distributions of ozone internal variability in the MLS and in the refC2 scenario are virtually identical, suggesting that the refC2 noise provides a credible estimate of the real-world internal variability.

S/N analysis of ozone changes

Here we use model-simulated internal variability noise to assess whether the forced ozone response has emerged. This assessment is performed for individual months and heights ('local' analysis) and for the 'overall' month-height pattern.

Figure 3d shows the local S/N ratio inferred from the WACCM for a trend length of 14 years (2005 to 2018). It represents the local signal in the WACCM ensemble mean (Fig. 1d) divided by the local noise in the WACCM refC2 run (Fig. 2b). In Fig. 3c, the mean forced signal from the WACCM is replaced by the MLS observed trend, which contains both the forced response and the internal variability. A larger local S/N ratio indicates increased likelihood that the ozone trend is anthropogenically forced. On the basis of the WACCM S/N for the refC2 scenario, the beginning of ozone recovery (as a forced response to combined GHG

and ODS forcing) can be detected with high confidence by 2018 in certain months and heights. In the upper stratosphere, recovery is much larger than internal variability in every month except during winter, when it propagates to the mid-stratosphere owing to polar descent. There is also a relative maximum in local S/N in September in the lower stratosphere in the MLS and in the WACCM ensemble mean. The overall pattern of local S/N is similar in the CCMI but statistical significance is lower in several key regions (Extended Data Fig. 4). This is expected given that the multi-model CCMI noise does not reflect intrinsic variability alone and is larger than in the WACCM single model.

To explore the impact of the post-2018 exceptional events, we performed a local S/N analysis over a longer period (2005–2023; see Extended Data Fig. 5). The month-height local S/N pattern over 2005–2023 shows many features similar to those in Fig. 3c,d, but also pronounced differences between the WACCM and the MLS, especially in the mid-stratosphere in October–December. LEs that account for the exceptional forcings^{15,16,32} would be expected to provide better agreement with the observed ozone trends.

We also performed a S/N analysis using the overall month-height fingerprint pattern of Antarctic ozone trends since 2005 (see Fig. 4). The element-wise covariance between the observed trend pattern (Fig. 1c) and model ensemble-mean forced response (Fig. 1d,e), at varying trend lengths, is divided by the spread of the covariance between individual noise patterns and the ensemble-mean responses (see Methods). Our results indicate that, for the period 2005–2018, the observed time-space structure of ozone changes over Antarctica is consistent with time-evolving ODS and GHG forcing. The observed changes during this period are inconsistent with natural internal variability alone (at the 5% significance level for the observed MLS pattern projected on both the WACCM and the CCMI month-height fingerprints). Although the exceptional years in and after 2020 lower the overall S/N, MLS trends projected on WACCM results (which neglect these events) nonetheless remain significant at the 10% significance level as late as the end of 2023.

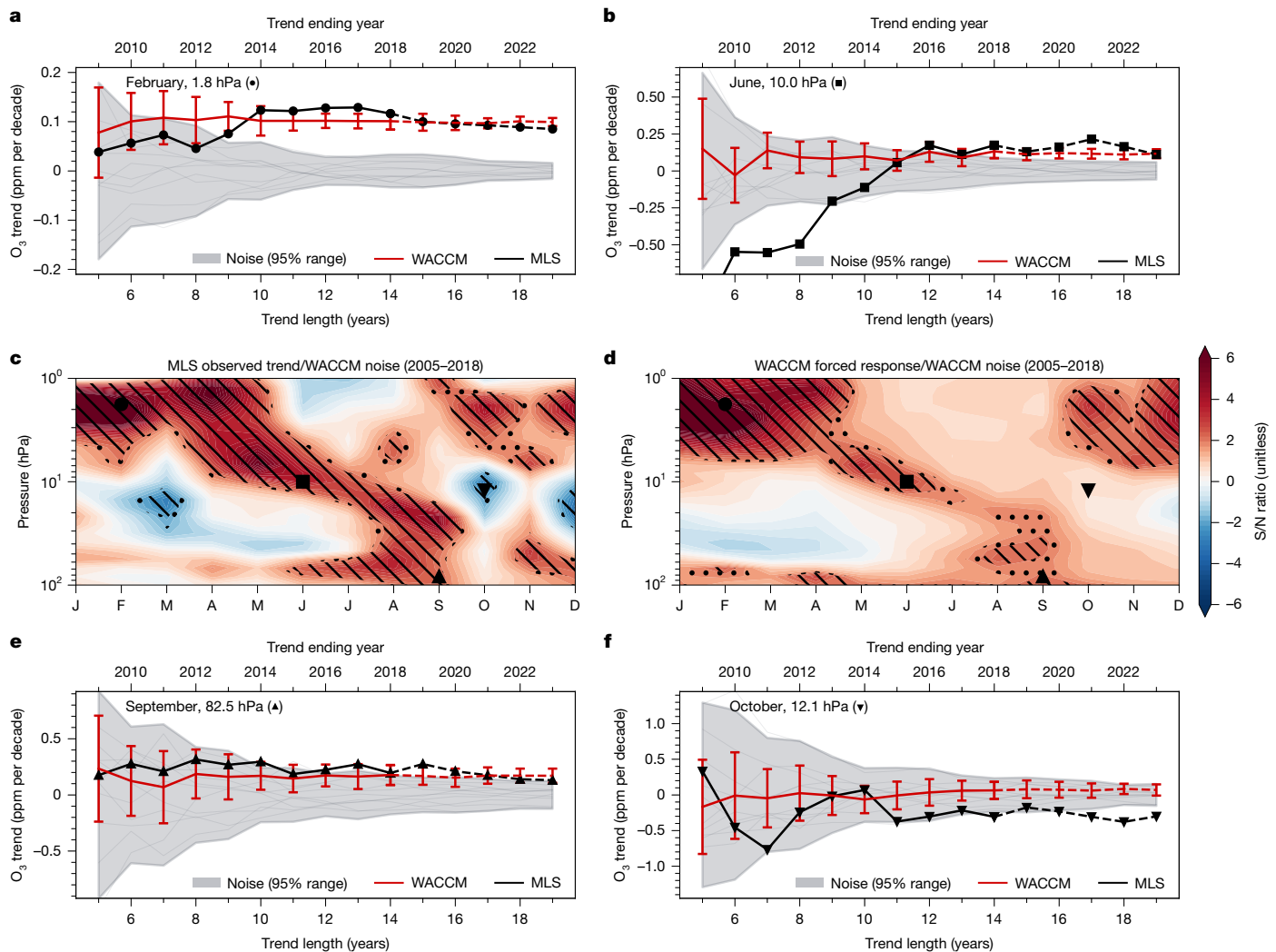


Fig. 3 | The local S/N pattern of ozone changes. The middle panels show the month–height patterns of the observed ozone trends in the MLS (c) and the WACCM ten-member ensemble mean refC2 ozone trends (d) divided by the internal variability noise in refC2 trends (which are given in Fig. 2b). Results are for trends over 2005–2018; Extended Data Fig. 5 similarly shows local S/N for trends calculated over 2005–2023. Hatched regions indicate that the local trend is significantly outside the noise at the 5% (backslashes) and 10% (dots)

levels. The top and bottom rows (panels a, b, e and f) provide the local signal and noise as a function of trend length at the same four illustrative months/heights shown in Fig. 1. The thin grey lines are the trends resulting from internal variability in each model realization and the grey shading indicates the 95% range of the realization spread. Thick lines are the trends from the MLS (black) and the WACCM ensemble mean (red). The error bars on the red line indicate ± 1 standard deviation in the ten-member ensemble.

We also project the observed pattern onto the GHG-only and ODS-only runs from the WACCM. Despite the fact that ozone has a nonlinear response to the coupled GHG and ODS forcing in the upper stratosphere³⁴, the linear addition in the covariance between the MLS and the separate GHG and ODS fingerprints is close to the coupled GHG + ODS results for the entire month–height domain in our analysis (see Fig. 4). This linear additivity enables us to estimate the relative contributions of GHG and ODS forcings in explaining the pattern similarity between observations and the coupled GHG + ODS fingerprint. The higher S/N values for the MLS trends projected onto the ODS fingerprint compared with the GHG fingerprint suggest that the observed pattern is dominated by the forced response to decreasing ODS concentrations. Compared with GHG, ODS-only forcing explains greater than 50% more pattern covariance with the MLS after 2014 (also visually illustrated in Extended Data Fig. 2). Indeed, the contribution of ODS-only forcing to the observed pattern in explaining the coupled GHG + ODS fingerprint differs significantly from internal variability noise at the 10% (and, in some years, 5%) significance level after 2014.

Antarctic springtime total ozone recovery

Signs of total column ozone (TCO) recovery are often sought during the Antarctic spring⁴, the season in which the ozone hole maximizes in depth and extent. In September, the emergence of ozone recovery occurs around 2018 both in terms of ozone at a single illustrative level (82.5 hPa) in Fig. 3e and in terms of the TCO in Extended Data Fig. 6a, in which the observed TCO is from the Ozone Monitoring Instrument (OMI)³⁷. Even with exceptionally low ozone in and after 2020, the total ozone healing signal from the satellite data is still significantly outside the internal variability noise (at the 10% level) in September.

A recent study raises the concern that October ozone in the mid-stratosphere has substantially decreased²⁰. However, this time and location is subject to only a small healing signal and shows substantial internal variability (see Fig. 3d,f), implying that trends with weak statistical significance here may well be spurious. Further, we note that, because low ozone concentrations are mainly confined within the polar vortex³⁸, vortex variations (for example, changes in size, shape and position) can contribute to ozone internal variability when concentrations

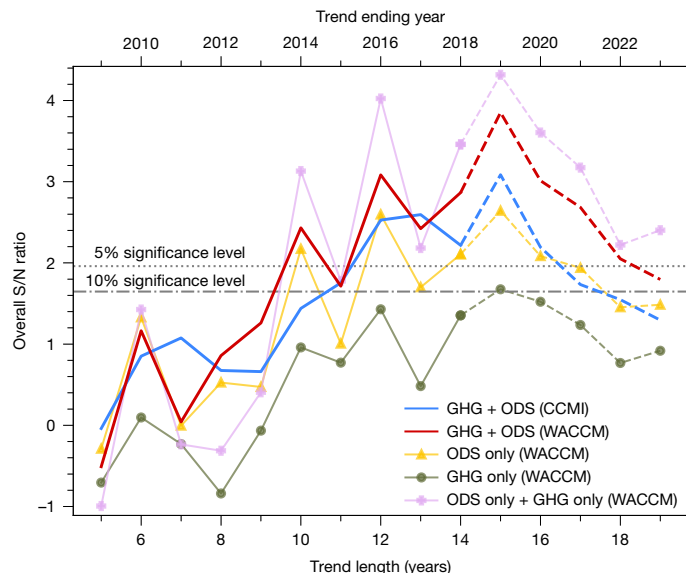


Fig. 4 | S/N characteristics for the overall month-height fingerprint pattern. The numerator of the S/N ratio is the element-wise covariance in the overall month-height ozone trend patterns between the MLS and the ensemble means of the coupled GHG + ODS runs from the WACCM (red) or the CCMI (blue), calculated at trend lengths ranging from 5 to 19 years. The denominator of the ratio is the standard deviation of the element-wise covariance computed between individual noise patterns and the ensemble-mean responses. The observed MLS ozone trend pattern is also projected onto the ODS-only and GHG-only fingerprints from the WACCM, shown in yellow and dark green, respectively (a linear addition of these two separate forcing results is shown by the mauve line). An overall S/N value above the grey dashed or dash-dotted lines indicates that the similarity between the observed month-height pattern and the model-predicted forced response pattern (to GHG, ODS or combined GHG + ODS changes) is significant at the 5% or 10% level, respectively, and is therefore unlikely to be explained by internal variability alone.

are spatially averaged over a fixed latitude range. This is especially important for months and heights when the vortex is often asymmetric (for example, October in the mid-stratosphere). For example, maps of ozone anomalies and vortex locations in October at 12.1 hPa (for which a strong ozone decrease was reported in a recent study²⁰) in Extended Data Fig. 7 illustrate how a shift of the vortex off the pole affects how it is sampled when using spatial averages calculated with fixed latitudinal boundaries (for example, for a simple comparison with satellite coverage). The reported large negative ozone trend in October in the mid-stratosphere²⁰ is greatly reduced when considering the vortex-averaged ozone (see Extended Data Fig. 8).

The emergence of column ozone recovery in October and November owing to combined ODS and GHG forcing (based on the WACCM ensemble-mean signal) had been expected around 2021 under typical conditions (Extended Data Fig. 6b,c). However, the unusually low ozone years in and after 2020 may have delayed detection in the observations. This underscores the importance of maintaining a long observation record to ensure high confidence in detecting and attributing future ozone changes at this time of year.

Summary and outlook

We performed a pattern-based fingerprint analysis for Antarctic ozone recovery, analogous to fingerprinting anthropogenic climate change^{5–12}. Our S/N results for local and overall pattern similarity between the MLS and single-model or multi-model ensembles provide high confidence that observed Antarctic ozone trends are primarily responses to ODS forcing rather than natural variability.

Further, we have shown that the amplitude of lower-stratospheric ozone variability is markedly enhanced in a present-day simulation relative to the amplitude of ozone variability in a ‘pre-ozone depletion’ simulation. It is crucial to consider this modulation of internal variability when evaluating the statistical significance of ozone trends. Furthermore, this enhancement in ozone variability owing to ODS forcings sheds light on a potential pathway for external forcing to modulate specific modes of natural internal variability, such as the Southern Annular Mode³⁹.

A marked ODS-driven signal of local ozone recovery in October and November has yet to emerge in the observations, probably because of the exceptionally low ozone years in and after 2020. These low ozone years are at least partly because of known volcanic and wildfire forcings not included in the available simulations. Although October ozone exhibits a decreasing trend in the mid-stratosphere²⁰, this negative trend is notably mitigated by using a different coordinate system that accounts for vortex variations.

Some caveats of the current analysis should be noted. Only one model with ten members is examined in detail in this work. To improve confidence in the D&A of forced responses versus natural variability in future ozone recovery assessments, it would be beneficial to use larger initial-condition ensembles from several single models rather than relying on single realizations from many different models^{11,23,24}. The forced response in this study considers GHGs and ODSs only and does not include known forcings from important volcanoes and large wildfires after 2012; future ensemble runs including these forcings would probably improve the consistency of the simulated and observed ozone changes. The projected long-lasting stratospheric water vapour from the Hunga eruption^{18,40} or future volcanic or wildfire forcing^{41,42} could reduce the future ozone recovery signal. Indeed, even the large S/N ratio we now see in the upper stratosphere could be temporarily obscured by uncertainties in future GHG emissions⁴³ and solar proton events⁴⁴.

Our work shows how fingerprinting and pattern similarity establish quantitative confidence that Antarctic ozone recovery has begun. It also indicates why it is crucial to maintain global height-resolved observations over extended periods to identify signal patterns that emerge from background noise, raising concerns about the impending satellite data gap in stratospheric measurements⁴⁵. A long observational record can ensure that estimated S/N ratios are less sensitive to short-term episodic perturbations, thereby providing high confidence in detecting and attributing trends⁵.

Online content

Any methods, additional references, Nature Portfolio reporting summaries, source data, extended data, supplementary information, acknowledgements, peer review information; details of author contributions and competing interests; and statements of data and code availability are available at <https://doi.org/10.1038/s41586-025-08640-9>.

1. Farman, J. C., Gardiner, B. G. & Shanklin, J. D. Large losses of total ozone in Antarctica reveal seasonal ClO_x/NO_x interaction. *Nature* **315**, 207–210 (1985).
2. Solomon, S., Garcia, R. R., Rowland, F. S. & Wuebbles, D. J. On the depletion of Antarctic ozone. *Nature* **321**, 755–758 (1986).
3. Laube, J. C. & Tegtmeier, S. in *Scientific Assessment of Ozone Depletion: 2022 Ch. 1* 111–114 (World Meteorological Organization, 2022).
4. Chipperfield, M. P. & Santee, M. L. in *Scientific Assessment of Ozone Depletion: 2022 Ch. 4* 215–270 (World Meteorological Organization, 2022).
5. Santer, B. D. et al. Exceptional stratospheric contribution to human fingerprints on atmospheric temperature. *Proc. Natl. Acad. Sci.* **120**, e2300758120 (2023).
6. Terray, L. et al. Near-surface salinity as nature’s rain gauge to detect human influence on the tropical water cycle. *J. Clim.* **25**, 958–977 (2012).
7. Stott, P. A., Sutton, R. T. & Smith, D. M. Detection and attribution of Atlantic salinity changes. *Geophys. Res. Lett.* **35**, L21702 (2008).
8. Gillett, N. P., Fyfe, J. C. & Parker, D. E. Attribution of observed sea level pressure trends to greenhouse gas, aerosol, and ozone changes. *Geophys. Res. Lett.* **40**, 2302–2306 (2013).
9. Christidis, N. & Stott, P. A. Changes in the geopotential height at 500 hPa under the influence of external climatic forcings. *Geophys. Res. Lett.* **42**, 10,798–10,806 (2015).

10. Shi, J.-R., Santer, B. D., Kwon, Y.-O. & Wijffels, S. E. The emerging human influence on the seasonal cycle of sea surface temperature. *Nat. Clim. Change* **14**, 364–372 (2024).
11. Santer, B. D. et al. Robust anthropogenic signal identified in the seasonal cycle of tropospheric temperature. *J. Clim.* **35**, 6075–6100 (2022).
12. Hasselmann, K. Optimal fingerprints for the detection of time-dependent climate change. *J. Clim.* **6**, 1957–1971 (1993).
13. Santee, M. L. et al. Prolonged and pervasive perturbations in the composition of the Southern Hemisphere midlatitude lower stratosphere from the Australian New Year's fires. *Geophys. Res. Lett.* **49**, e2021GL096270 (2022).
14. Bernath, P., Boone, C. & Crouse, J. Wildfire smoke destroys stratospheric ozone. *Science* **375**, 1292–1295 (2022).
15. Solomon, S. et al. Chlorine activation and enhanced ozone depletion induced by wildfire aerosol. *Nature* **615**, 259–264 (2023).
16. Wang, X. et al. Stratospheric climate anomalies and ozone loss caused by the Hunga Tonga-Hunga Ha'apai volcanic eruption. *J. Geophys. Res. Atmos.* **128**, e2023JD039480 (2023).
17. Zhang, J. et al. Chemistry contribution to stratospheric ozone depletion after the unprecedented water-rich Hunga Tonga eruption. *Geophys. Res. Lett.* **51**, e2023GL105762 (2024).
18. Wohltmann, I., Santee, M. L., Manney, G. L. & Millán, L. F. The chemical effect of increased water vapor from the Hunga Tonga-Hunga Ha'apai eruption on the Antarctic ozone hole. *Geophys. Res. Lett.* **51**, e2023GL106980 (2024).
19. Manney, G. L. et al. Siege in the southern stratosphere: Hunga Tonga-Hunga Ha'apai water vapor excluded from the 2022 Antarctic polar vortex. *Geophys. Res. Lett.* **50**, e2023GL103855 (2023).
20. Kessenich, H. E., Seppälä, A. & Rodger, C. J. Potential drivers of the recent large Antarctic ozone holes. *Nat. Commun.* **14**, 7259 (2023).
21. Hassler, B. & Young, P. J. in *Scientific Assessment of Ozone Depletion: 2022 Ch. 3* 153–214 (World Meteorological Organization, 2022).
22. Santer, B. D. et al. Accounting for the effects of volcanoes and ENSO in comparisons of modeled and observed temperature trends. *J. Geophys. Res. Atmos.* **106**, 28033–28059 (2001).
23. Dhomse, S. S. et al. Estimates of ozone return dates from Chemistry-Climate Model Initiative simulations. *Atmos. Chem. Phys.* **18**, 8409–8438 (2018).
24. Zeng, G. et al. Attribution of stratospheric and tropospheric ozone changes between 1850 and 2014 in CMIP6 models. *J. Geophys. Res. Atmos.* **127**, e2022JD036452 (2022).
25. Robertson, F. et al. Signal-to-noise calculations of emergence and de-emergence of stratospheric ozone depletion. *Geophys. Res. Lett.* **50**, e2023GL104246 (2023).
26. Deser, C. et al. Insights from Earth system model initial-condition large ensembles and future prospects. *Nat. Clim. Change* **10**, 277–286 (2020).
27. Waters, J. W. et al. The Earth Observing System Microwave Limb Sounder (EOS MLS) on the Aura satellite. *IEEE Trans. Geosci. Remote Sens.* **44**, 1075–1092 (2006).
28. Morgenstern, O. et al. Review of the global models used within phase 1 of the Chemistry-Climate Model Initiative (CCMI). *Geosci. Model Dev.* **10**, 639–671 (2017).
29. Marsh, D. R. et al. Climate change from 1850 to 2005 simulated in CESM1(WACCM). *J. Clim.* **26**, 7372–7391 (2013).
30. Garcia, R. R., Smith, A. K., Kinnison, D. E., de la Cámara, Á. & Murphy, D. J. Modification of the gravity wave parameterization in the Whole Atmosphere Community Climate Model: motivation and results. *J. Atmos. Sci.* **74**, 275–291 (2017).
31. Wargan, K., Weir, B., Manney, G. L., Cohn, S. E. & Livesey, N. J. The anomalous 2019 Antarctic ozone hole in the GEOS Constituent Data Assimilation System with MLS observations. *J. Geophys. Res. Atmos.* **125**, e2020JD033335 (2020).
32. Solomon, S. et al. Emergence of healing in the Antarctic ozone layer. *Science* **353**, 269–274 (2016).
33. Manabe, S. & Wetherald, R. T. Thermal equilibrium of the atmosphere with a given distribution of relative humidity. *J. Atmos. Sci.* **24**, 241–259 (1967).
34. Haigh, J. D. & Pyle, J. A. Ozone perturbation experiments in a two-dimensional circulation model. *Q. J. R. Meteorol. Soc.* **108**, 551–574 (1982).
35. Molina, M. J. & Rowland, F. S. Stratospheric sink for chlorofluoromethanes: chlorine atom-catalysed destruction of ozone. *Nature* **249**, 810–812 (1974).
36. Solomon, S., Portmann, R. W., Sasaki, T. & Hofman, D. J. Four decades of ozonesonde measurements over Antarctica. *J. Geophys. Res. Atmos.* **110**, D21311 (2005).
37. Levelt, P. F. et al. The ozone monitoring instrument. *IEEE Trans. Geosci. Remote Sens.* **44**, 1093–1101 (2006).
38. Schoeberl, M. R. & Hartmann, D. L. The dynamics of the stratospheric polar vortex and its relation to springtime ozone depletions. *Science* **251**, 46–52 (1991).
39. Thompson, D. W. J. et al. Signatures of the Antarctic ozone hole in Southern Hemisphere surface climate change. *Nat. Geosci.* **4**, 741–749 (2011).
40. Zhou, X. et al. Antarctic vortex dehydration in 2023 as a substantial removal pathway for Hunga Tonga-Hunga Ha'apai water vapor. *Geophys. Res. Lett.* **51**, e2023GL107630 (2024).
41. Eric Klobas, J., Wilmouth, D. M., Weisenstein, D. K., Anderson, J. G. & Salawitch, R. J. Ozone depletion following future volcanic eruptions. *Geophys. Res. Lett.* **44**, 7490–7499 (2017).
42. Chim, M. M. et al. Climate projections very likely underestimate future volcanic forcing and its climatic effects. *Geophys. Res. Lett.* **50**, e2023GL103743 (2023).
43. Revell, L. E., Bodeker, G. E., Huck, P. E., Williamson, B. E. & Rozanov, E. The sensitivity of stratospheric ozone changes through the 21st century to N_2O and CH_4 . *Atmos. Chem. Phys.* **12**, 11309–11317 (2012).
44. Stone, K. A., Solomon, S. & Kinnison, D. E. On the identification of ozone recovery. *Geophys. Res. Lett.* **45**, 5158–5165 (2018).
45. Chipperfield, M. P. & Bekki, S. Opinion: Stratospheric ozone – depletion, recovery and new challenges. *Atmos. Chem. Phys.* **24**, 2783–2802 (2024).

Publisher's note Springer Nature remains neutral with regard to jurisdictional claims in published maps and institutional affiliations.

Springer Nature or its licensor (e.g. a society or other partner) holds exclusive rights to this article under a publishing agreement with the author(s) or other rightsholder(s); author self-archiving of the accepted manuscript version of this article is solely governed by the terms of such publishing agreement and applicable law.

© The Author(s), under exclusive licence to Springer Nature Limited 2025

Article

Methods

Satellite data

The MLS provides daily observations since August 2004 and the data have been extensively validated^{46,47}. Here we use MLS version 5 monthly mean level 3 ozone mixing ratios on pressure coordinates from 100 hPa to 1 hPa. The level 3 product covers latitudes from 82° S to 82° N, using a 4° latitude bin. Ozone is averaged over 66° S–82° S in this paper, weighted by cosine latitude to account for the reduction in area further poleward. We use the monthly mean values starting from 2005 (excluding the second half of 2004) so that every month in the trend analysis has the same number of time samples.

Satellite TCO observations are from the OMI³⁷ version 3 daily level 3 product, which is aboard the same satellite as the MLS. TCO from the OMI is also averaged by month starting from 2005 and in the latitude range from 66° S to 82° S (weighted by cosine latitude).

Model and scenario descriptions

A total of 19 different models participated in the CCM1-1, with a total of 33 realizations for the refC2 scenario^{23,28}. This scenario characterizes ODS emissions following the World Meteorological Organization (WMO)⁴⁸ and other GHG emissions following RCP6.0 (ref. 49) from 1960 to 2100. To prevent biasing towards models with more ensemble members, we only use the first realization from each model.

We also used the fully coupled CESM1-WACCM4 (refs. 29,30) in this analysis, which incorporates coupled ocean–atmosphere processes with interactive chemistry. Our primary focus is on a ten-member WACCM initial-condition ensemble generated with the same refC2 scenario used by the CCM1-1 models. As well as refC2, we consider three other WACCM initial-condition ensembles, referred to as fODS, fGHG and historical. fODS (also referred to as the GHG-only runs) fixes ODS forcing at the 1960 level, whereas GHG concentrations evolve as in the refC2 runs. Alternatively, fGHG (or ODS-only runs) fixes GHG concentrations in 1960, whereas ODS levels evolve as in refC2 runs. The historical scenario involves temporal changes in both GHGs and ODSs from 1955 to 1979 (ref. 50). The CCM1 and WACCM simulations are vertically interpolated to MLS pressure levels (linear interpolation in log pressure) and are also averaged over 66° S–82° S and cosine-weighted for consistency with the MLS.

Although the WACCM runs analysed here are less than 30 years in length (from 1995 to 2024 for refC2, fODS and fGHG and from 1955 to 1979 for the historical scenario), an advantage of the set of simulations is that each scenario has ten realizations that are slightly perturbed in their initial conditions⁵¹. This facilitates reliable estimation of both the underlying forced response (the ensemble mean) and internal variability. By contrast, multi-model ensembles convolve internal variability estimates with inter-model differences or errors in forced responses and/or with model differences in the amplitude and patterns of internal variability^{26,51,52}. For example, not all of the 19 CCM1 models are fully coupled to an interactive ocean²⁸, probably introducing large cross-model differences in forced responses and natural variability.

As shown here, the WACCM historical and refC2 initial-condition ensembles can also be used to explore whether external forcing modulates internal variability—a key issue in signal detection. Relative to multiple linear regression approaches for estimating the anthropogenic component of ozone trends, using the WACCM fully coupled chemistry climate model has the advantage that no previous assumptions are required about the relationships between different predictor variables (such as the El Niño–Southern Oscillation, Southern Annular Mode, quasi-biennial oscillation, solar cycle etc.). As in the real world, nonlinear interactions between ozone and climate internal variability can be present in the model simulations.

Although large initial-condition ensembles from several single models are preferred for analysing the interactions between atmospheric chemistry and natural internal variability, the high computational

cost may be a barrier to generating such ensembles, at least for some models²⁶.

Signal and noise definition and uncertainty estimation

The ‘local’ signal and noise denotes an analysis at individual months and heights. We define the local signal as the linear trend in ozone (starting in 2005, ending years can vary from 2009 to 2023) at each month and pressure level, derived from a linear fit to ensemble-mean ozone data from forced model simulations. To calculate the ‘local’ noise, we first subtract the ensemble-mean ozone time series from each individual model realization; the resulting residuals then characterize the internal variability²⁶. Noise is defined as the standard deviation of the ozone trends (with the same trend length as the signal) in these residuals. The noise represents the spread in ozone trends that is primarily the result of internal variability. Both the local signal and the local noise have units of ppm per decade (parts per million by volume per decade). The statistical significance of ozone trends is determined by the local S/N ratio. For two-tailed tests, a 5% (10%) significance level is associated with local S/N values larger than 1.96 (1.645).

As well as the local S/N analysis at individual months and heights, we also applied a conventional ‘fingerprint’ method⁵ to the overall simulated and observed month–height patterns of ozone changes. The key point here is that the entire month–height pattern is used to distinguish a forced response from internal variability. The overall signal is the element-wise uncentred covariance between the month–height ozone trend patterns in the MLS (for example, Fig. 1c) and in the WACCM ensemble mean (for example, Fig. 1d) or between the trend pattern in the MLS and the CCM1 multi-model mean (for example, Fig. 1e), at varying trend lengths. This is essentially equivalent to projecting the observed month-resolved and height-resolved trend pattern onto the forced response⁵. The overall noise is the standard deviation in the similarly computed uncentred covariance but between internal variability in individual realizations (obtained from the different panels in Extended Data Fig. 1 after removing the ensemble mean) and the mean forced response. Fingerprinting is performed over the same space–time ranges used in the local S/N analysis: that is, using spatially averaged ozone changes between 66° S and 82° S at altitudes from 100 hPa to 1 hPa and in the 12 months from January to December. The increase in the overall S/N in Fig. 4 with increasing trend length suggests that the observed overall month–height ozone change pattern is unlikely to be explained by internal variability alone.

Vortex coverage and vortex-averaged ozone calculation

Vortex coverage (shown as the dots in Extended Data Fig. 7) and vortex-averaged ozone (red lines in Extended Data Fig. 8) are obtained from the MLS daily level 2 and the derived meteorological products (DMPs)^{53–55}. The DMPs are calculated from the NASA Global Modeling and Assimilation Office (GMAO) using meteorology from the Modern-Era Retrospective analysis for Research and Applications, Version 2 (MERRA-2) and are interpolated to the same time and location as the MLS level 2 products. Vortex edge in the MLS is determined by a height-dependent scaled potential vorticity (sPV) threshold⁵⁶ on potential temperature (theta) surfaces. For consistency with our other results shown in pressure levels, we vertically interpolated this sPV threshold from the theta level to the pressure level (linear interpolation from log theta to log pressure) and applied it to the daily level 2 ozone from the MLS and daily level 2 sPV from the DMPs. The monthly mean polar vortex coverage at each grid point on the MLS level 3 grid (with 4° × 5° horizontal resolution) is averaged using daily vortex coverage, defined as the fraction of sPV in each grid box that meets the vortex threshold⁵⁶ against the total number of MLS overpasses in that grid box every day. Similarly, for vortex-averaged ozone, we only average the MLS level 2 observed ozone (weighted by cosine latitude) when its associated sPV (from the DMPs) meets the vortex threshold⁵⁶ on a daily basis in each grid box for every month.

Data availability

MLS and OMI satellite data are publicly available at <https://disc.gsfc.nasa.gov>. CCM model outputs are available at <https://archive.ceda.ac.uk> and the CESM model outputs are available at <https://www.earth-systemgrid.org>. All of the pre-processed model data (for example, monthly mean ozone averaged over 66° S–82° S from the CCM and the WACCM and interpolated onto the MLS vertical coordinates) are available at Zenodo (<https://doi.org/10.5281/zenodo.14497873>)⁵⁷.

Code availability

The code used to generate all of the figures in this analysis is available at Zenodo (<https://doi.org/10.5281/zenodo.14497873>)⁵⁷.

46. Hubert, D. et al. Ground-based assessment of the bias and long-term stability of 14 limb and occultation ozone profile data records. *Atmos. Meas. Tech.* **9**, 2497–2534 (2016).
47. Froidevaux, L. et al. Validation of Aura Microwave Limb Sounder stratospheric ozone measurements. *J. Geophys. Res. Atmos.* **113**, D15S20 (2008).
48. World Meteorological Organization (WMO). *Scientific Assessment of Ozone Depletion: 2010* (World Meteorological Organization, 2011).
49. Meinshausen, M. et al. The RCP greenhouse gas concentrations and their extensions from 1765 to 2300. *Clim. Change* **109**, 213 (2011).
50. Stone, K. A., Solomon, S., Thompson, D. W. J., Kinnison, D. E. & Fyfe, J. C. On the Southern Hemisphere stratospheric response to ENSO and its impacts on tropospheric circulation. *J. Clim.* **35**, 1963–1981 (2022).
51. Kay, J. E. et al. The Community Earth System Model (CESM) large ensemble project: a community resource for studying climate change in the presence of internal climate variability. *Bull. Am. Meteorol. Soc.* **96**, 1333–1349 (2015).
52. Solomon, A. et al. Distinguishing the roles of natural and anthropogenically forced decadal climate variability: implications for prediction. *Bull. Am. Meteorol. Soc.* **92**, 141–156 (2011).
53. Manney, G. L. et al. Solar occultation satellite data and derived meteorological products: sampling issues and comparisons with Aura Microwave Limb Sounder. *J. Geophys. Res. Atmos.* **112**, D24S50 (2007).

54. Millán, L. F. et al. Multi-parameter dynamical diagnostics for upper tropospheric and lower stratospheric studies. *Atmos. Meas. Tech.* **16**, 2957–2988 (2023).
55. Manney, G. L. et al. Jet characterization in the upper troposphere/lower stratosphere (UTLS): applications to climatology and transport studies. *Atmos. Chem. Phys.* **11**, 6115–6137 (2011).
56. Lawrence, Z. D., Manney, G. L. & Wargan, K. Reanalysis intercomparisons of stratospheric polar processing diagnostics. *Atmos. Chem. Phys.* **18**, 13547–13579 (2018).
57. Wang, P. et al. Data and code for “Fingerprinting the Recovery of Antarctic Ozone”. Zenodo <https://doi.org/10.5281/zenodo.14497873> (2024).

Acknowledgements We thank C. Deser and P. Lin for helpful discussions. We also thank L. Horowitz and M. Lin for providing GFDL model data for this analysis. S.S. and P.W. gratefully acknowledge support from the Atmospheric Chemistry division of the National Science Foundation under grant nos. 2316980 and 2128617. B.D.S. was supported by the Francis E. Fowler IV Center for Ocean and Climate at Woods Hole Oceanographic Institution (WHOI). D.E.K. was financed in part by NASA grant 80NSSC19K0952. Q.F. was supported in part by NSF grant AGS-2202812. The Community Earth System Model (CESM) project is supported by the National Science Foundation and the Office of Science of the U.S. Department of Energy. We gratefully acknowledge high-performance computing support from Cheyenne (<https://doi.org/10.5065/D6RX99HX>) provided by NCAR’s Computational and Information Systems Laboratory (CISL), sponsored by the National Science Foundation. Work at the Jet Propulsion Laboratory, California Institute of Technology, was carried out under a contract with the National Aeronautics and Space Administration (NASA; 80NM0018D0004).

Author contributions P.W., S.S. and B.D.S. designed the study. D.E.K. designed and performed the WACCM simulations. P.W. analysed the data and produced the figures. P.W. and S.S. drafted the initial text. B.D.S., Q.F., K.A.S., J.Z., G.L.M. and L.F.M. contributed substantially to the interpretation of findings.

Competing interests The authors declare no competing interests.

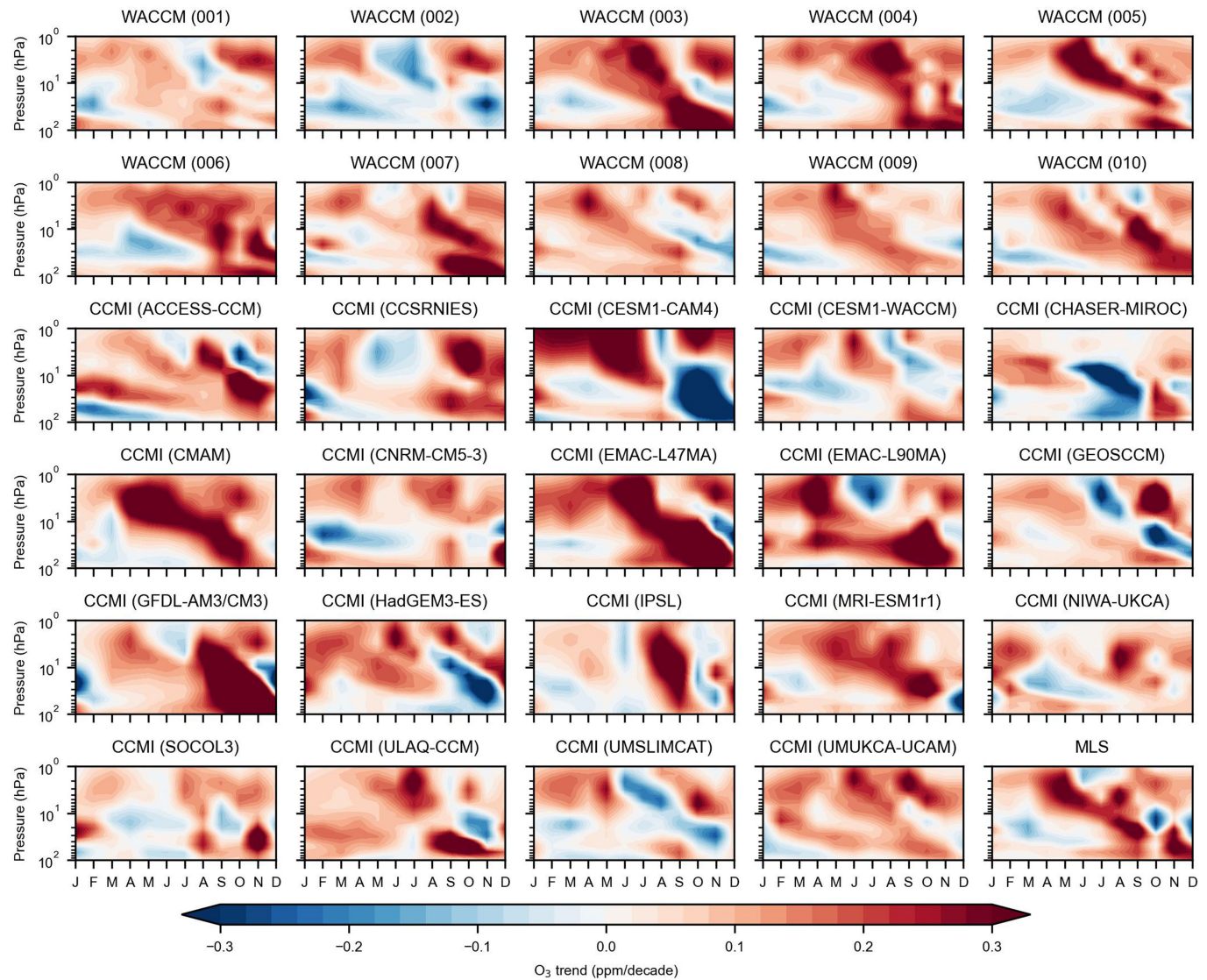
Additional information

Correspondence and requests for materials should be addressed to Peidong Wang or Susan Solomon.

Peer review information *Nature* thanks Wolfgang Steinbrecht and the other, anonymous, reviewer(s) for their contribution to the peer review of this work.

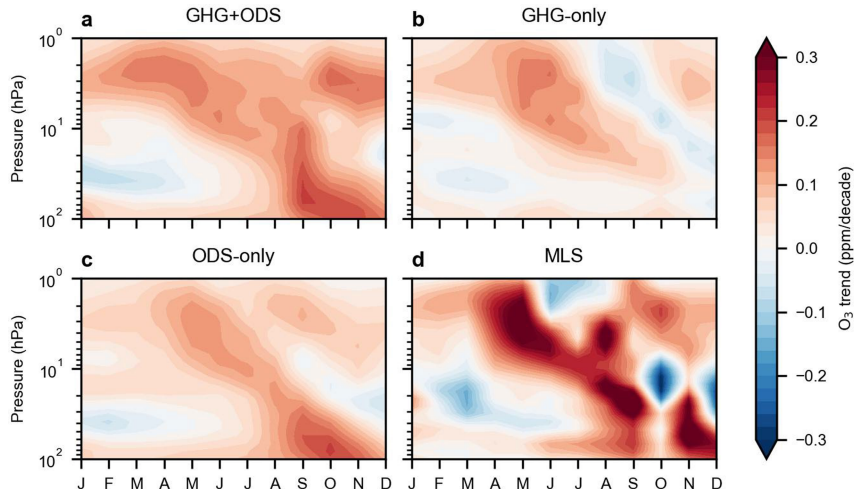
Reprints and permissions information is available at <http://www.nature.com/reprints>.

Article



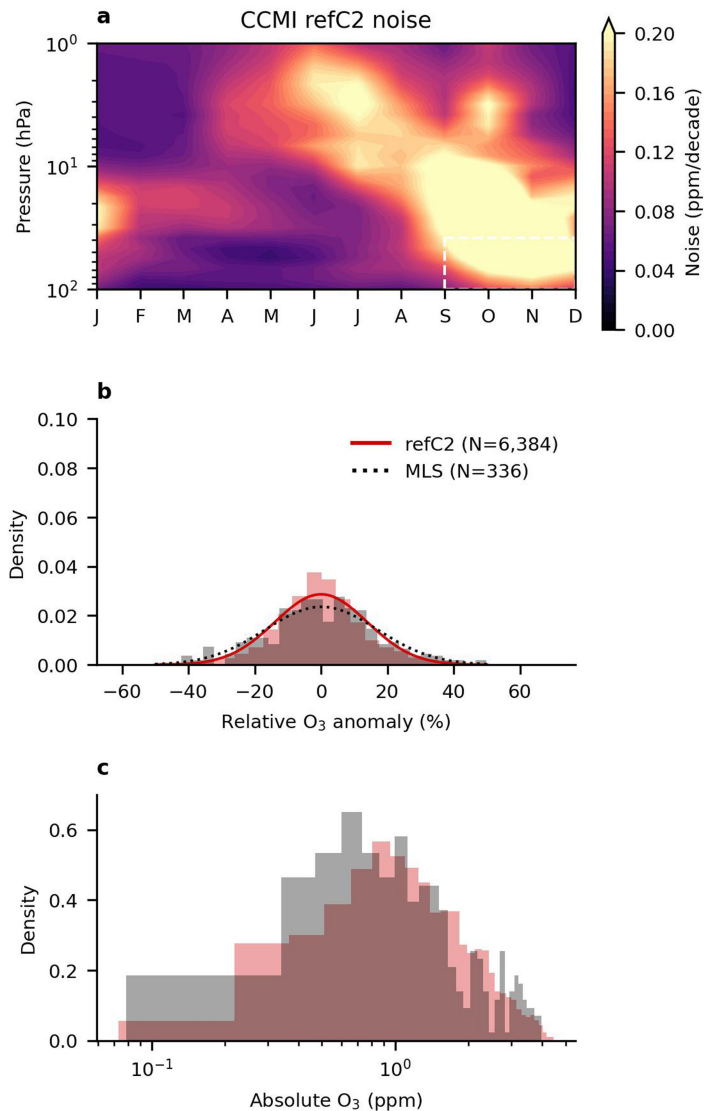
Extended Data Fig. 1 | Variability superimposed on external forcing. Ozone trends from 2005–2018 in individual WACCM realizations (top two rows, with the realization number indicated in the title of each panel) and in individual

models from the CCM1-1 (last four rows, with model names indicated in the title of each panel) under the refC2 scenario. The MLS observed trend is shown in the bottom-right panel.



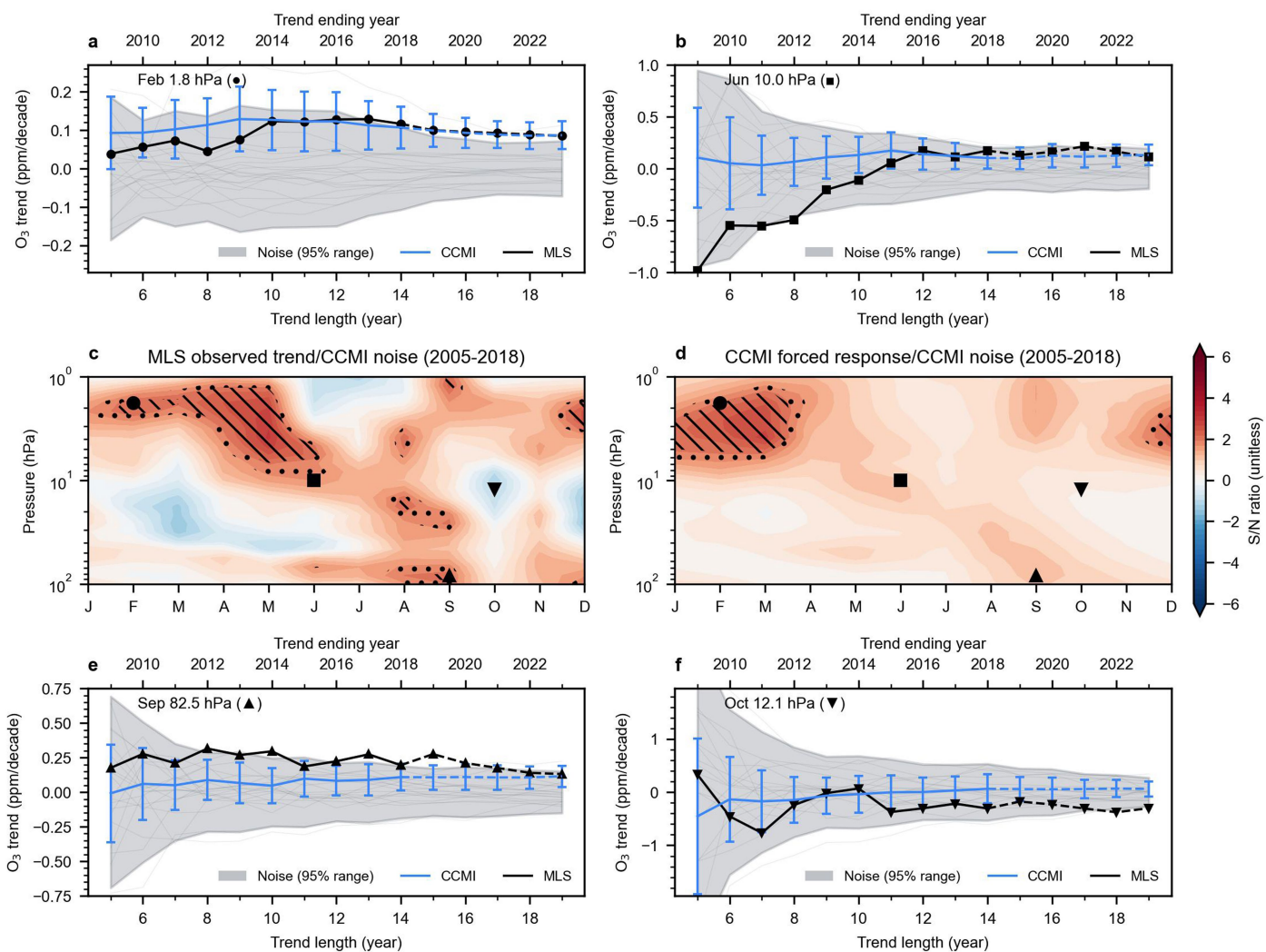
Extended Data Fig. 2 | Ozone trends owing to different forcings. Ensemble-mean ozone trends (2005–2018) averaged over ten WACCM members for each scenario. Results indicate the forced responses in ozone owing to: combined time-evolving GHG and ODS forcing (refC2) (a), evolving GHG forcing only

(fODS) (b) and evolving ODS forcing only (fGHG) (c). A detailed description of each scenario is given in Methods. The observed ozone trend from the MLS in 2005–2018 is also shown in panel d for visual comparison with forced ozone trends owing to different forcings.


Extended Data Fig. 3 | Ozone variability modulated by external forcing.

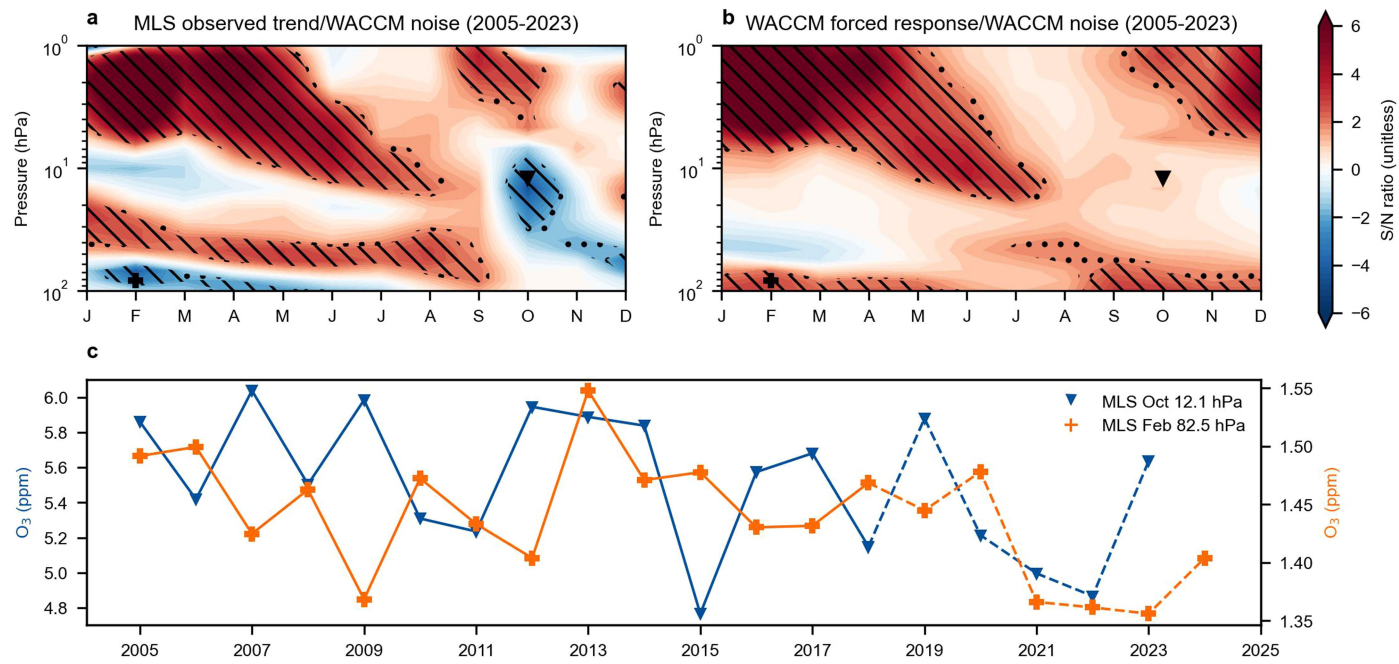
Similar to Fig. 2 but for the CCMC models. Note that the spread in ozone trends in the CCMC arises not only from internal variability but also from cross-model differences and errors (discussed in detail in Methods). This convolving of

internal variability with model differences and errors contributes to the larger noise in panel **a** compared with the noise derived from the WACCM single-model refC2 ensemble in Fig. 2b.



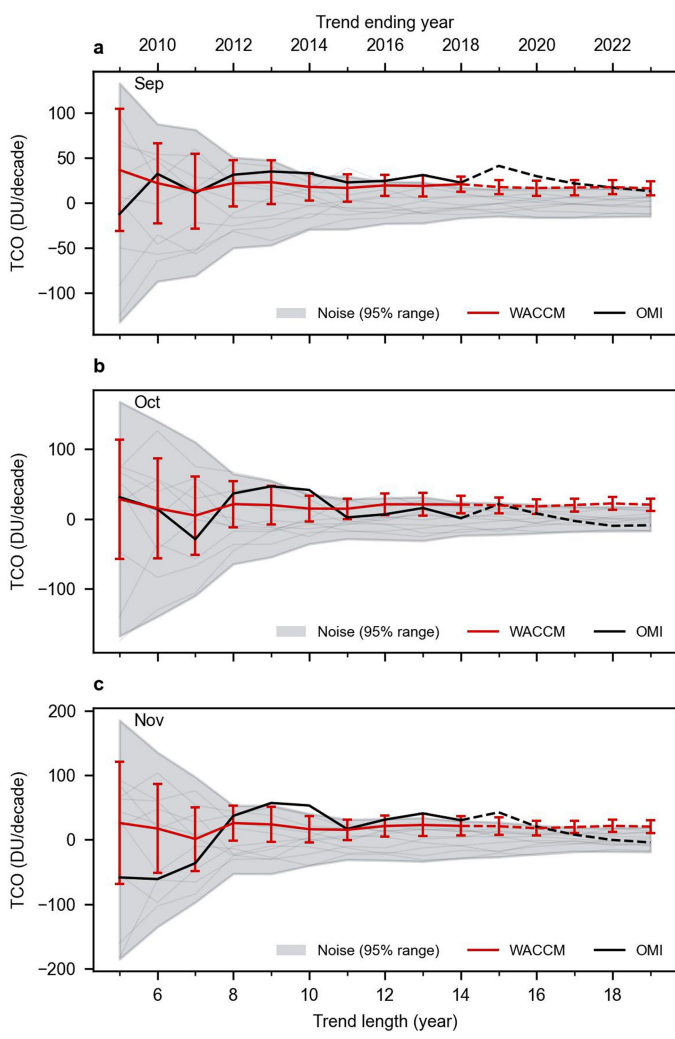
Extended Data Fig. 4 | The local S/N characteristics of ozone changes. Similar to Fig. 3 but with results for the CCMI models.

Article



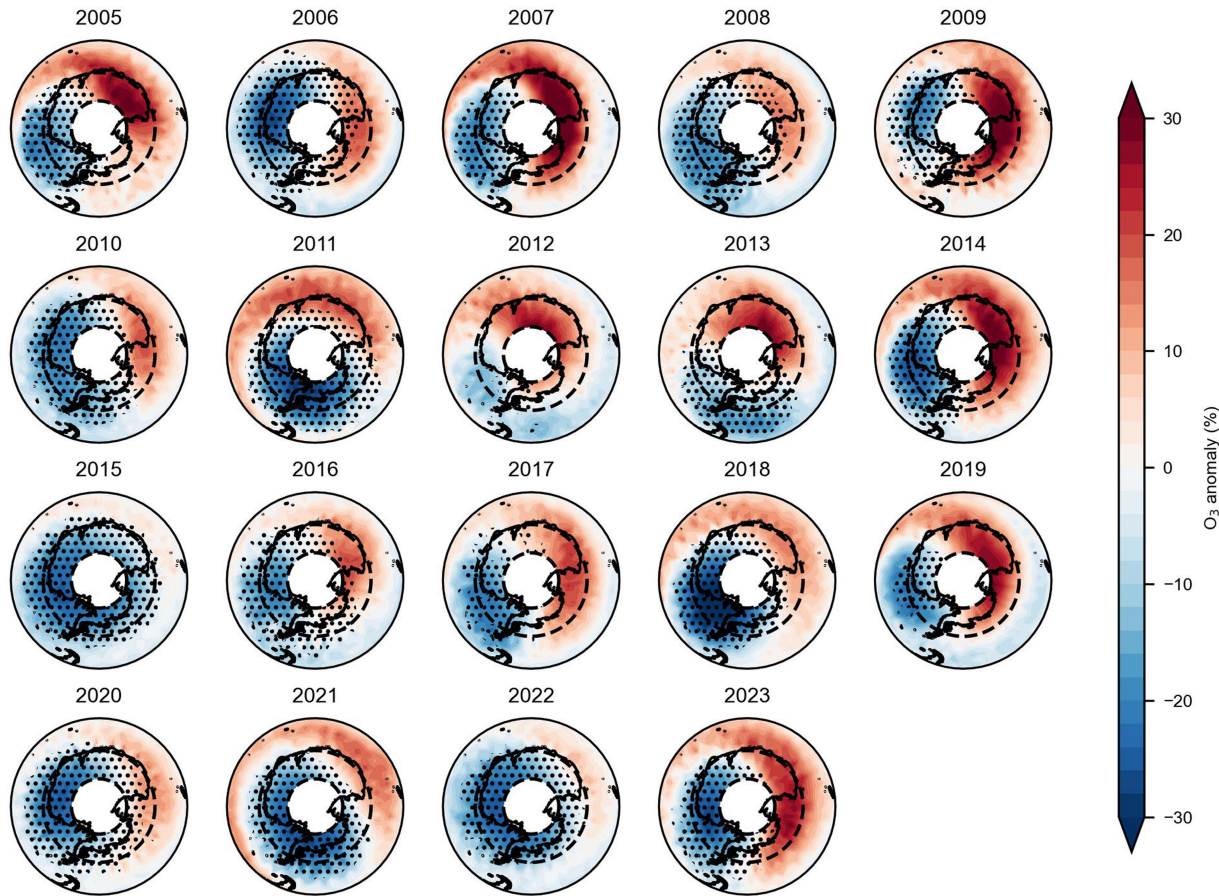
Extended Data Fig. 5 | The local S/N pattern of ozone changes. Similar to Fig. 3 but for signal and noise estimates based on ozone trends over 2005–2023 (rather than over 2005–2018). There is a marked decrease in the MLS ozone in October and November in the mid-stratosphere and in January to May in the lowermost stratosphere. This raises the question of whether these two features

may be linked. The bottom panel shows the time series of ozone mixing ratios from the MLS in October at 12.1 hPa (blue) and in February at 82.5 hPa (orange). The decrease in February at 82.5 hPa is mainly because of continued low ozone after 2021 (panel c), which lags the behaviour in October by about a season, suggesting that they may be linked.



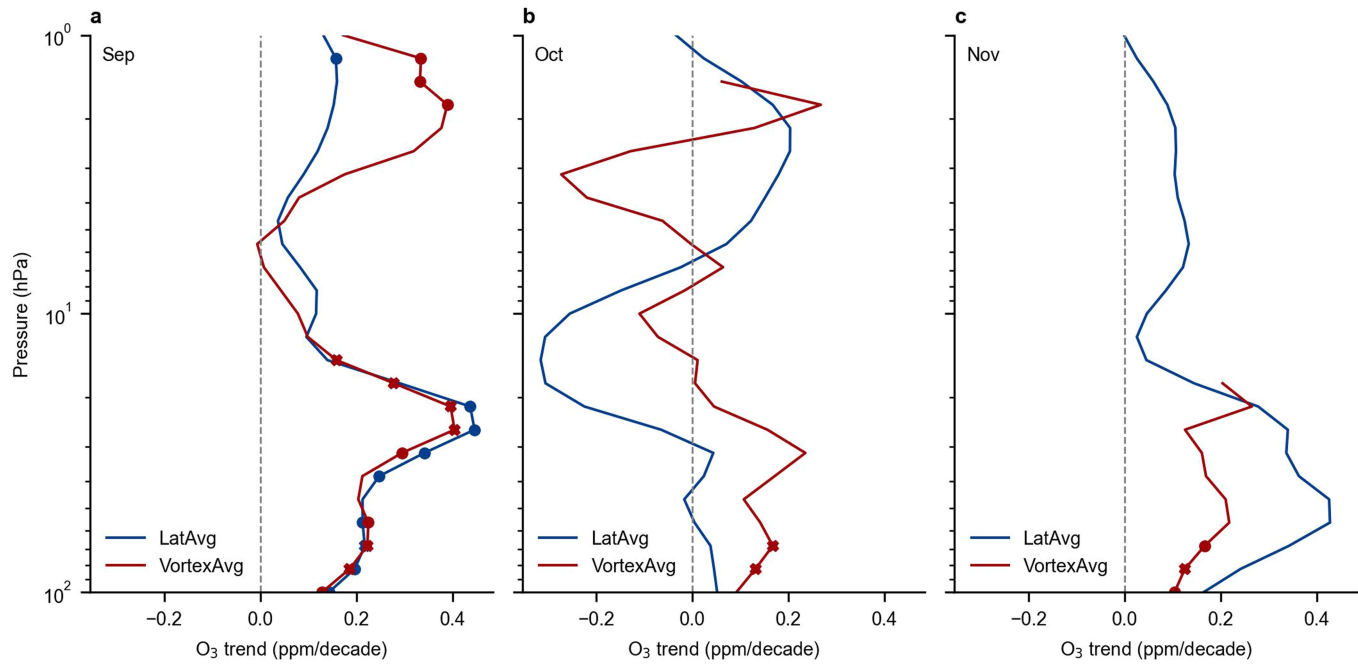
Extended Data Fig. 6 | Time of emergence of springtime TCO recovery.

Similar to the top and bottom panels in Fig. 3 except the trends are the TCO from the WACCM and the OMI.



Extended Data Fig. 7 | Map of the MLS ozone anomalies and polar vortex in October at 12.1 hPa. The colour shadings indicate the ozone anomaly relative to the zonal mean in 2005–2018. Because the location of the polar vortex can

vary considerably over time, dotted markers indicate that the polar vortex has occupied a given grid box for more than 25% of the time in that month. Black dashed lines encompass the area between latitudes 66° S and 82° S.



Extended Data Fig. 8 | MLS springtime ozone trends (2005–2018) using fixed latitude averages versus vortex averages. Monthly mean ozone trends in September, October and November from 2005 to 2018 are shown as blue lines (in which ozone is averaged across fixed latitudes between 66° S and 82° S) and red lines (in which ozone is averaged inside the polar vortex) at different

pressure levels. A detailed description of the vortex calculation is provided in Methods. Dots and crosses indicate trends significant at the 5% and 10% levels, respectively. Note that the statistical confidence in this figure is based solely on *P*-values from linear regression. It does not rely on internal variability noise generated by the WACCM or the CCM3 model, as shown in the other figures.